Journal of Materials Chemistry A

Coherent Magnetic Nanoinclusions Induce Charge Localization in Half-Heusler Alloys Leading to High-Tc Ferromagnetism and Enhanced Thermoelectric Performance

Journal:	*Journal of Materials Chemistry A*
Manuscript ID	TA-ART-01-2019-001156.R1
Article Type:	Paper
Date Submitted by the Author:	13-Mar-2019
Complete List of Authors:	Lu, Ruiming; University of Michigan, Department of Materials Science and Engineering Lopez, Juan; University of Michigan, Department of Materials Science and Engineering Liu, Yuanfeng; University of Michigan, Department of Materials Science and Engineering Bailey, Trevor; University of Michigan, Department of Physics Page, Alexander; University of Michigan, Department of Physics Wang, Si; Wuhan University of Technology, State Key Laboratory of Advanced Technology for Materials Synthesis and Processing; University of Michigan, Department of Physics Uher, Ctirad; University of Michigan, Department of Physics Poudeu, Pierre Ferdinand; University of Michigan, Department of Materials Science and Engineering; University of Michigan, Department of Materials Science and Engineering

Coherent Magnetic Nanoinclusions Induce Charge Localization in Half-Heusler Alloys Leading to High-*T*c Ferromagnetism and Enhanced Thermoelectric Performance

R. Lu,[a] J. Lopez,[a] Y. Liu,[a] T. P. Bailey,[b] A. A. Page, [b] S. Wang, [b,c] C. Uher, [b] P. F.P. Poudeu [a,*]

[a] Laboratory for Emerging Energy and Electronic Materials, Department of Materials Science and Engineering, University of Michigan, Ann Arbor, MI, 48109, USA.

[b] Department of Physics, University of Michigan, Ann Arbor, MI, 48109, USA.

[c] State Key Laboratory of Advanced Technology for Materials Synthesis and Processing, Wuhan University of Technology, Wuhan, Hubei 430070, China.

KEYWORDS: Thermal conductivity, nanostructuring, ferromagnetic semiconductor, half-Heusler, thermoelectrics.

ABSTRACT: Performance improvement traditionally realized through a combination of power factor optimization via electronic doping and lattice thermal conductivity reduction using nanostructuring have reached their optimal limits in many leading thermoelectric materials, making further enhancement in the thermoelectric figure of merit extremely challenging. Here, a novel approach to electronic transport engineering using coherent magnetic nanoinclusions is demonstrated. It was found that the incorporation of coherent magnetic full-Heusler(FH) nanoinclusions ($Ti(Ni_{4/3}Fe_{2/3})Sn$) into a half-Heusler(HH) matrix ($Ti_{0.25}Zr_{0.25}Hf_{0.5}NiSn_{0.975}Sb_{0.025}$) with optimal doping level and lattice thermal conductivity leads to high Curie temperature ferromagnetism (T_c ~ 650 K) along with a large reduction in the effective carrier density within the HH matrix. It is believed that the embedded magnetic FH nanoinclusions interact with the spin of itinerant carriers, leading to charge localization and the formation of overlapping bound magnetic polarons (BMPs). This gives rise to significant enhancements of both carrier mobility and thermopower, which minimizes the reduction in the overall power factor, simultaneously with a large drop in the total thermal conductivity owing to the reduction of the electronic contribution to the thermal conductivity. The implementation of magnetic nanoinclusions strategy in a variety of state-of-the-art thermoelectric materials could pave the way towards even larger figures of merit.

Introduction

Thermoelectric (TE) materials research have continued to attract vast attention over several decades due to their ability to promote energy conversion between heat and electricity and their great potential in energy recycling, such as in automotive and industrial waste heat recovery. These intensive research activities led to the development of several materials optimization concepts. This includes the successful application of the concept of nanostructuring in thermoelectrics that has accelerated the development of high performance TE materials owing to significant suppression of the thermal conductivity that arises from enhanced phonon scattering at high-density interfaces (phase and grain boundaries) within the samples. [1-6 5,7-10]

However, limited enhancements in the TE performance, as measured by the dimensionless figure of merit, $zT = \sigma S^2 T/\kappa$; where σ, S, κ, and T are respectively, the electrical conductivity, Seebeck coefficient, thermal conductivity, and the absolute temperature, are expected through the application of the nanostructuring concept alone, due to the existence of lower limits to thermal conductivities of materials, the so-called glass limits κ_g.[11-21] The thermal conductivities of some leading thermoelectric materials under investigation are already approaching their glass limits,[15-21] while their figure of merit zT still does not ensure efficiency $\eta = \frac{\Delta T\sqrt{1+ZT}-1}{T_h\sqrt{1+ZT}+\frac{T_c}{T_h}}$ comparable to that of other energy conversion technologies, such as photovoltaics.[22,23] Additionally, electron scattering will become severe as grains are refined to sizes as small as few nanometers,[3,24,25] comparable to the mean free path of electrons. Therefore, the benefit from the suppressed thermal conductivity may be counteracted by the degradation in electrical transport, giving marginal improvement in the figure of merit. As a result, further significant enhancements in the thermoelectric performance should include optimization of the electronic parameters, i.e., electrical conductivity σ and Seebeck coefficient S. However, it is challenging to improve both parameters simultaneously since they are adversely coupled by the carrier concentration.[11] Recently, band engineering,[11,26-29] modulation doping,[30-33] energy filtering,[34-37] etc., have been reported as appropriate strategies to tailor the electronic properties of TE materials. Traditionally, it was thought that magnetism would not benefit thermoelectric performance and could even be detrimental due to localization effects and/or enhanced electron scattering by magnetic moments. However, Tsujii and Mori pointed out that strong interactions between extrinsic carriers and magnetic moments could potentially yield a large Seebeck coefficient, as they found in $CuFeS_2$, by enhancing charge carrier effective mass.[38-41] Recently, improved thermoelectric performance have been achieved through suppression of intrinsic charge carrier excitations using the magnetic transition of embedded particles.[38-41]

Previously, our group introduced the concept of atomic scale structural engineering of thermoelectrics (ASSET),[36,37] as an elegant approach to achieve simultaneous enhancement in the power factor and reduction in the thermal conductivity using suitable nanoinclusions that are coherently embedded within the matrix. We successfully demonstrated the fabrication of nanocomposites consisting of a HH matrix with coherently embedded ultrafine full-Heusler (FH) inclusions.[36,37,42] Significant Seebeck enhancements have been achieved in HH/FH nanocomposites that are generally attributed to the screening of low-energy carriers by the electronic energy band offset built at the interfaces between the nanoscale FH and the HH matrix.[37,42] Chai *et al.* have systematically studied the structural evolution of HH by HRTEM when introducing extra Ni and concluded that the FH phases form because of clustering of extra Ni, which confirms the results from theoretical calculations[43,44] and is also consistent with the structural atomic diffusion configuration initially proposed for the ASSET concept.[36] Phase segregation has an important effect on the transport properties in the HH alloys as has already been demonstrated in HH/FH composites. Another important phase separation process occurring in the HH alloys with general composition $Ti_xZr_yHf_{1-x-y}NiSn$ is the formation of Ti-rich and Ti-poor phases with HH structure when the amount of Ti exceeds the solubility limit in the Zr(Hf)-based HH alloy.[45-48]

In this study, we investigate the interplay between both types of phase segregation in $Ti_{0.25}Zr_{0.25}Hf_{0.5}NiFe_xSn_{0.975}Sb_{0.025}$ HH/FH composites obtained through incorporation of various amounts of elemental Fe into a HH matrix with optimized doping level.[47] It is anticipated that the added elemental Fe will fill in tetrahedral vacancies within the HH crystal lattice, enabling the formation of nanoscale inclusions with FH structure within the HH matrix via a similar reaction mechanism previously proposed for the Ni-incorporated HH systems.[36,37] By adjusting the Fe concentration, one can tune the density and average particle size of Fe-containing FH (Fe-FH) inclusions within the composites. Meanwhile, phase separation into Ti-rich and Ti-poor phases with HH structure is also anticipated in $Ti_{0.25}Zr_{0.25}Hf_{0.5}NiSn_{0.975}Sb_{0.025}$, given the high substitution level of Ti beyond the solubility limit of Ti in Zr(Hf)-based HH alloys.[45,46,49-52] Here, we report that the incorporation of coherent magnetic nanoinclusions (Fe-FH) into half-Heusler (HH) alloys with optimized doping level ($Ti_{0.25}Zr_{0.25}Hf_{0.5}NiFe_xSn_{0.975}Sb_{0.025}$) induces charge localization and formation of overlapping bound magnetic polarons leading to (1) high-T_c ferromagnetism along with (2) enhanced thermoelectric figure of merit owing to the drastic reduction of the effective carrier density, large increase in the carrier mobility and Seebeck coefficient, as well as a significant decline in the

electronic contribution to the thermal conductivity. We attempt to rationalize the interesting electronic transport and magnetic properties resulting from the multiscale engineering of the internal structure of heavily doped $Ti_{0.25}Zr_{0.25}Hf_{0.5}NiFe_xSn_{0.975}Sb_{0.025}$ HH/FH composites by integrating the concepts of the energy filtering effect at nanoscale FH/HH interfaces[34-37] with charge carrier localization by nanoscale magnetic FH inclusions embedded within the HH matrix.

Experimental details

Synthesis. To synthesize $Ti_{0.25}Zr_{0.25}Hf_{0.5}(Ni,Fe_x)Sn_{0.975}Sb_{0.025}$ (x = 0-0.15) composites, elemental powders of high purity were weighed and thoroughly mixed using agate pestle and mortar under Ar atmosphere in a glove box. The mixed powder was then loaded into a quartz tube and sealed under residual pressure of 10^{-3} Torr. The powder was heated at 400 °C for 24 hours and subsequently heated at 900 °C for 300 hours. The resultant powder after solid-state reaction was ground, sealed in a quartz tube, and further annealed at 900 °C for another 168 hours to make sure the starting elements are thoroughly reacted. High-density pellets were obtained by sintering the powder from solid-state reaction at 900 °C for 1 hour under an applied pressure of 100 MPa using a uniaxial hot press. The pellets were subsequently well polished and cut into different pieces for various measurements of electronic and thermal properties. Rectangular bars with approximate dimensions of 3 × 3 × 10 mm^3 cut perpendicular to the pressing direction were used for thermopower and electrical resistivity measurements. Additional rectangular bars specimen with approximate dimensions 1 × 3 × 8 mm^3 cut in the same direction were used for Hall effect measurement. Disk shape pellets of 10 mm in diameter and ~ 2 mm in thickness cut in a direction perpendicular to the pressing direction were used for thermal conductivity measurement along the direction parallel to the pressing direction. Although measured along different directions, the electronic and thermal properties represent that of the bulk sample owing to the cubic structure of half-Heusler alloys.

Characterization. The phase composition and crystal structure were characterized using powder X-ray diffraction (PXRD) patterns collected on a Rigaku rotating anode system operating at 40 kV and 100 mA using a monochromated Cu-K_α radiation source. The overall chemical composition of the synthesized composites was evaluated by wavelength dispersive spectroscopy (WDS) on Cameca SX100 Electron Probe Microanalyzer. The average composition of various phases within the composites was characterized using point analysis by electron probe microanalysis (EPMA). The microstructure was studied by transmission electron microscopy (TEM) on JEOL 3100R05 with a cold field emission gun and double Cs correction. Backscatter electron (BSE) images and energy dispersive spectrum (EDS) mapping were collected on JEOL JSM-7800FLV Scanning Electron Microscope equipped with Oxford XMaxN 80mm^2 silicon-drift energy-dispersive X-ray spectrometer. The electrical conductivity and Seebeck coefficient were measured simultaneously from room temperature to 773 K using the four-probe method on a commercial ULVAC-RIKO ZEM-3 system under a low-pressure helium atmosphere. The specific heat capacity and thermal diffusivity were measured on a laser flash system (Linseis LFA-1000) from room temperature to 773 K. The thermal conductivity was calculated by $\kappa = \rho C_P D$, where ρ, C_P and D are density, specific heat capacity and thermal diffusivity, respectively. The density of the pressed pellets was measured using Helium gas pycnometry on Micromeritics Accupyc II 1340. Low temperature and high temperature Hall measurement were carried out under a magnetic field of 1 T on a home-built apparatus to evaluate the carrier concentration and mobility. The magnetic moment data were collected using a Quantum Design MPMS-CL SQUID magnetometer. DC magnetic moment under field cooled (FC) and zero-field cooled (ZFC) conditions were measured on powder of samples of selected $Ti_{0.25}Zr_{0.25}Hf_{0.5}(Ni,Fe_x)Sn_{0.975}Sb_{0.025}$ compositions over a temperature range of 2-800 K with an applied field of 100 Oe.

Results and discussion

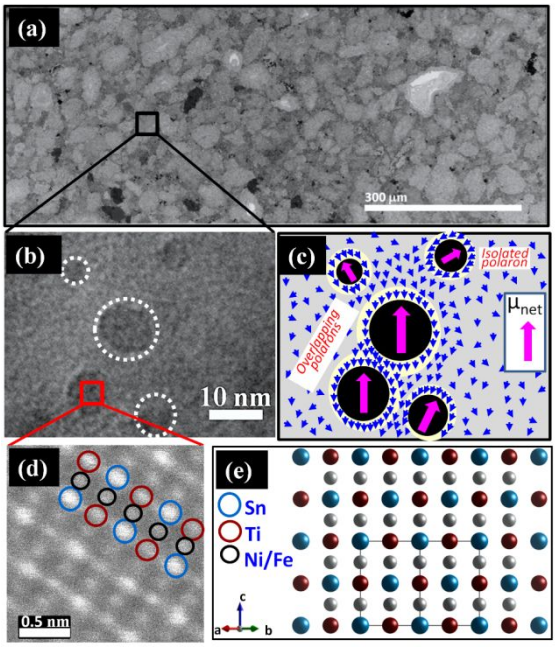

Figure 1: Microstructure of $Ti_{0.25}Zr_{0.25}Hf_{0.5}(Ni,Fe_{0.05})Sn_{0.975}Sb_{0.025}$ composites: (a) SEM image showing micron scale (Ti,Fe)-rich (black) and (Zr,Hf)–rich (grey) grains; (b) HRTEM image of a (Zr,Hf)-rich grain showing the presence of nanometer scale (Ti,Fe)-rich inclusions; (c) schematic illustration of bound magnetic polarons (BMPs) formed through magnetic interactions between magnetic (Ti,Fe)-rich inclusions in (b) and itinerant electrons; (d) atomic scale resolution image of one of the (Ti,Fe)-rich inclusions in (b) showing the FH structure; (e) a schematic representation of the (110) plane of a FH structure.

Structure and composition. Several compositions of the $Ti_{0.25}Zr_{0.25}Hf_{0.5}(Ni,Fe_x)Sn_{0.975}Sb_{0.025}$ (x = 0-0.15) HH/(Fe-FH) composites were synthesized by solid state reaction of the elements and structurally characterized using scanning electron microscopy (SEM), high-resolution transmission electron microscopy (HRTEM) and powder X-ray diffraction (PXRD), which confirmed both the formation of nanoinclusions with FH structure (**Figure 1**) and phase separation of the HH matrix into Ti-rich and (Zr,Hf)-rich HH phases (**Figure S1 to S3**). In addition, composition mapping and EPMA (electron probe microanalysis) point analysis (**Table S1**) revealed the coexistence in various $Ti_{0.25}Zr_{0.25}Hf_{0.5}(Ni,Fe_x)Sn_{0.975}Sb_{0.025}$ compositions of a Ti-rich FH phase with composition $Ti(Ni_{4/3}Fe_{2/3})Sn$ along with Zr-rich and Hf-rich HH phases. It is interesting to note from the EPMA result (**Table S1**) that while the $Ti_{0.25}Zr_{0.25}Hf_{0.5}NiSn_{0.975}Sb_{0.025}$ HH composition naturally phase separates into Ti-rich and (Zr,Hf)-rich phases, the added Fe tends to mix exclusively with the Ti phase to form (Ti,Fe)-rich nanoinclusions ($Ti(Ni_{4/3}Fe_{2/3})Sn$) with the FH structure embedded within the (Zr,Hf)-rich HH matrix. As the Fe content in the starting mixture increases, the population density and average size of the (Ti,Fe)-rich FH phase, $Ti(Ni_{4/3}Fe_{2/3})Sn$, within the resulting composites increase (**Figure S3** and **Table S1-S2**) whereas the fraction of Ti within the matrix decreases according to the chemical equation (1).

$$0.25\ Ti + 0.25\ Zr + 0.5\ Hf + Ni + Sn + x\ Fe \rightarrow 3x/2\ Ti(Ni_{4/3}Fe_{2/3})Sn\ (FH\ inclusion) + [Ti_{(0.25-1.5x)}Zr_{0.25}\ Hf_{0.5}]Ni_{(1-2x)}Sn_{(1-1.5x)}\ (HH\ matrix) \quad (1)$$

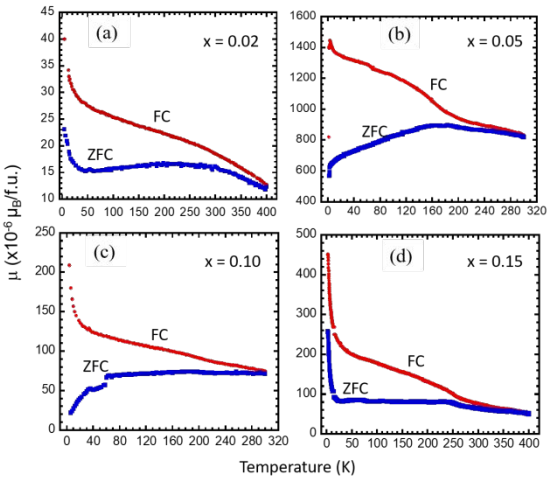

Figure 2: Temperature dependent magnetization of $Ti_{0.25}Zr_{0.25}Hf_{0.5}(Ni,Fe_x)Sn_{0.975}Sb_{0.025}$ composites under Field-cooled (FC, red circles) and zero-field cooled (ZFC, blue squares) conditions: (a) x = 0.02; (b) 0.05; (c) x = 0.1; (d) x = 0.15.

The proposed chemical equation is consistent with elemental mapping showing the distribution of various elements within the composites (**Figure S4**). It can be seen that the added elemental Fe preferentially incorporates into the Ti-rich phase (**Figure S4**) to form the $Ti(Ni_{4/3}Fe_{2/3})Sn$ phase. The chemical composition of the FH inclusion phase was confirmed by EPMA point analysis result (**Table S1**), and the FH atomic structure of the $Ti(Ni_{4/3}Fe_{2/3})Sn$ inclusion phase was confirmed by the atomic resolution transmission electron microscopy image on the samples with x = 0.05 (**Figure 1d**).

The increased population density and average size of the (Ti, Fe)-rich FH phase upon increasing Fe incorporation into the HH matrix was further confirmed by BSE images (**Figure S3**). Processing the BSE images using Image-J software enabled an estimation of the mole fraction (ν_{obs}) of the (Ti, Fe)-rich phase observed in various samples, which is compared to the theoretical fraction (ν_{calc}) of (Ti, Fe)-rich calculated from the chemical equation (1) (**Table S2**). The discrepancy between the observed mole fraction (ν_{obs}) and the calculated mole fraction (ν_{calc}) of (Ti, Fe)-rich phase can be taken as an indirect measurement of the mole fraction of subnanometer scale (Ti,Fe)-rich phases within various samples. Remarkably, the discrepancy between the observed (ν_{obs}) and the predicted (ν_{calc}) mole fraction of the (Ti,Fe)-rich phase drastically decreases with the increasing Fe content, suggesting that as the nominal Fe content increases, the population density of (Ti,Fe)-rich nanoinclusions within the sample increases leading to agglomeration into larger particles. Within this picture, one can consider that ~78% of the (Ti,Fe)-rich phases formed in the sample with x = 0.05 are at the subnanometer scale (**Table S2**), whereas for the sample with x = 0.15 this number is only ~16%. Additional discussion of the microstructure of the synthesized materials is provided in the supplementary information.

The above described modulation of the microstructure and chemistry of various phases within the synthesized $Ti_{0.25}Zr_{0.25}Hf_{0.5}(Ni,Fe_x)Sn_{0.975}Sb_{0.025}$ composites upon incorporation of Fe is expected to profoundly influence their magnetic and thermoelectric properties.

Magnetic properties. Field cooled (FC) and zero-field cooled (ZFC) magnetic moment data of selected $Ti_{0.25}Zr_{0.25}Hf_{0.5}(Ni,Fe_x)Sn_{0.975}Sb_{0.025}$ composites collected under an applied field of 100 Oe showed that all Fe-containing samples display various degrees of magnetic interactions (**Figure 2**). Interestingly, the magnitude of the magnetic moment as well as the nature of magnetic ordering within various samples strongly depends on the Fe content, which, in turn, strongly affects the microstructure and chemistry of the resulting composites. For instance, the FC curve for the sample with x = 0.02 shows a gradual increase of the magnetic moment from ~12 $x10^{-6}$ μ_B/f.u. at 300 K to ~28 $x10^{-6}$ μ_B/f.u. at 40 K. Further dropping the temperature resulted in a drastic increase of the magnetic moment to ~40 $x10^{-6}$ μ_B/f.u. at 5 K. A similar trend is observed in the magnetic moment curves of the samples with x = 0.1 and 0.15. However, the magnitude of the magnetic moment at 300 K is enhanced

to ~80 x10^{-6} μ_B/f.u. for the sample with x = 0.1 and to ~90 x10^{-6} μ_B/f.u. for the sample with x = 0.15. The magnetic moment of the sample with x = 0.1 and 0.15 increases to ~120 x10^{-6} μ_B/f.u. and ~200 x10^{-6} μ_B/f.u., respectively, upon cooling to 40 K, then sharply rises to ~210 x10^{-6} μ_B/f.u. and

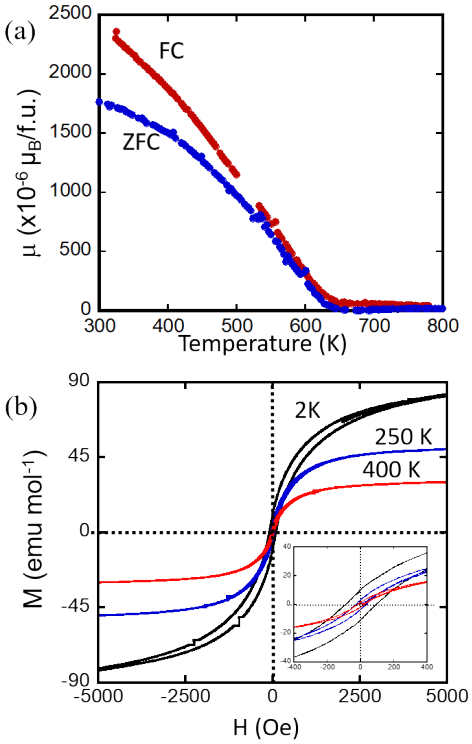

Figure 3: Magnetic behavior of $Ti_{0.25}Zr_{0.25}Hf_{0.5}(Ni,Fe_{0.05})Sn_{0.975}Sb_{0.025}$ composites: (a) temperature-dependent magnetic moment above 300 K showing the Curie transition temperature T_c ~ 650 K (FC: field cooled, red circles; ZFC: zero-field cooled, blue circles); (b) magnetization versus applied field at various temperatures between 2 K and 400 K. Inset of (b) is the enlarged detail of hysteresis near zero field to show the coercive force.

~460 x10^{-6} μ_B/f.u. at 5 K. The sample with x = 0.05 showed a unique trend with the largest value of the magnetic moment at 300 K, ~700 x10^{-6} μ_B/f.u., which reaches ~1440 x10^{-6} μ_B/f.u. upon cooling to 5 K.

The presence of magnetic ordering within various samples can be associated with the formation of the magnetically active (Ti,Fe)-rich FH nanoinclusions within the (Zr,Hf)-rich HH matrix. Indeed, a schematic illustration of the molecular orbital diagram for TiNiFeSn (**Figure S5**) reveals the presence of unpaired spins with a total spin value S = 2, suggesting some degree of magnetic ordering within the (Ti,Fe)-rich FH phase. However, the magnitude of the magnetic moment in the FH inclusion depends on the relative position of the bonding a_1 orbital with respect to the pair of degenerate bonding e_g (d_{z^2}, $d_{x^2-y^2}$) orbitals and the set of triple-degenerate bonding t_{2g} (d_{xy}, d_{yz}, d_{xz}) orbitals, which, in turn, can be altered by the change in the average size of the FH inclusions. For instance, in the bulk TiNiFeSn phase, one would anticipate the localization of the bonding a_1 orbital at energy levels below that of the bonding d-orbitals resulting in a total spin value S = 1.[53-55] Within this picture, one can rationalize the observed change in the magnitude of the magnetic moments of various samples by taking into account the average particle size as well as the distribution of (Ti,Fe)-rich FH within the HH matrix. The incorporation of low Fe content (x ≤ 0.05) resulted in the formation of widely dispersed nanometer scale (Ti,Fe)-rich FH inclusions (**Figure 1b**) with high spin state (S = 2) within the HH matrix, yielding the large magnetic moments observed in the sample with x = 0.05 (**Figure 2b**). Further increasing the Fe content beyond x > 0.05 gives rise to the agglomeration of nanometer scale (Ti,Fe)-rich FH inclusions into microscale particles (**Figure S3**) with bulk-like properties. Accordingly, the magnetic moments for the samples with x = 0.1 and 0.15 are much reduced compared to that of x = 0.05. The observed increase in the magnitude of magnetic moment of samples with x = 0.1 and 0.15 compared to that of the sample with x = 0.02 can be associated with the increase in the population density of the (Ti,Fe)-rich phase within the samples, as suggested by the SEM images (**Figure S3-S4**).

The complex shape of the magnetic moment curves (ZFC and FC) for various samples points to frustrated magnetic ordering. For instance, the divergence between the ZFC and the FC magnetic moment curves at temperatures below 300 K suggests the coexistence of ferromagnetic (FM) and/or anti-ferromagnetic (AFM) ordering in the samples, which leads to magnetic frustration.[53,56-58] While the sharp increase of the magnetic moment below 40 K can be attributed to AFM ordering, the apparent saturation of the ZFC magnetic moment below 200 K for samples with x = 0.02, 0.05 and 0.15 points to FM ordering (**Figure 2**). Notably, the FC magnetic moment of the sample with x = 0.05 above 300 K gradually decreases with rising temperature up to 650 K, at which point the moment drops to nearly zero (**Figure 3a**) and thereafter, remains constant with further increase in the temperature. Thus, $Ti_{0.25}Zr_{0.25}Hf_{0.5}(NiFe_{0.05})Sn_{0.975}Sb_{0.025}$ hosts predominantly FM behavior with T_c ~ 650 K.

The FM character of the sample with x = 0.05 was further confirmed through field-dependent magnetization measurements at selected temperatures between 2 K and 400 K (**Figure 3b**). The characteristic S-shape of the magnetization curves up to 400 K is consistent with FM ordering with saturation values decreasing from 100 emu/mol at 2 K to 30 emu/mol at 400 K. We attribute the high-T_c FM behavior to long-range coupling of localized moments on adjacent (Ti,Fe)-rich magnetic nanoinclusions within the (Zr,Hf)-rich semiconducting HH matrix via formation of overlapping bound magnetic polarons (BMPs)[54,55,59-66] and/or carrier-

mediated mechanisms (**Figure 1c**). The above described magnetic ordering of (Ti,Fe)-rich inclusions within the (Zr,Hf)-rich HH matrix is expected to strongly influence atomic scale electronic transport behavior in the synthesized composites.

Thermoelectric properties. One interesting unique characteristic of the synthesized $Ti_{0.25}Zr_{0.25}Hf_{0.5}(NiFe_x)Sn_{0.975}Sb_{0.025}$ composites is their multifunctional behavior, which is manifested by the coexistence of high T_c ferromagnetism and *n*-type heavily doped semiconductivity. As shown in **Figure 4**, the electrical conductivity at zero-field for all compositions gradually decreases with rising temperature, which is a typical behavior for heavily doped semiconductors. The temperature-dependent electrical conductivity data are well fit by the power law $T^{-\alpha}$, as expected for acoustic phonon scattering of charge carriers. Interestingly, the power law exponent decreases with the increasing Fe content from $\alpha \approx 0.70$ for the sample with x = 0 to $\alpha \approx 0.41$ for the sample with x = 0.15, which suggests a transition of the transport mechanism from metallic-like to semi-metal-like behavior, possibly due to variations of the charge carrier concentration in different samples (**Figure 4c**).

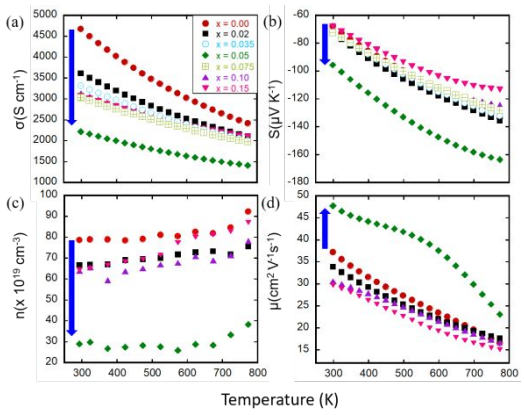

Figure 4: Electronic transport properties of $Ti_{0.25}Zr_{0.25}Hf_{0.5}(Ni,Fe_x)Sn_{0.975}Sb_{0.025}$ composites: (a) electrical conductivity; b) Seebeck coefficient; c) carrier concentration and d) carrier mobility

Regardless of the temperature, the magnitude of the electrical conductivity initially decreases with increasing Fe content, reaching minimum values for the composition with x = 0.05, then increases thereafter with further increase in the Fe content. However, the electrical conductivity of all Fe containing samples remains lower than that of the Fe-free HH matrix. For instance, the electrical conductivity at 300 K is ~ 4700 S/cm for the Fe-free sample (x = 0) and gradually decreases to ~ 3600 S/cm for the sample with x = 0.02 and further drop to ~ 3300 S/cm for the sample with x = 0.035 before reaching the minimum value of ~ 2200 S/cm for the sample with x = 0.05. The electrical conductivity of samples with x= 0.075, x = 0.1 and 0.15 showed a slight increase (~ 3100 S/cm at 300 K) compared to the sample with x = 0.05. The observed drop in the electrical conductivity upon incorporation of Fe atoms is attributed to the decrease in the charge carrier density, which, in turn, can be associated with (1) the energy filtering of low-energy carriers at the atomic scale interfaces between the HH matrix and FH inclusions as discussed elsewhere,[36,37,42,67,68] and/or (2) the localization of free carriers by magnetic (Ti,Fe)-rich FH inclusions embedded within the (Zr,Hf)-rich HH matrix. This analysis is consistent with the carrier density data (**Figure 4c**) extracted from the Hall coefficient data (**Figure S6a**), assuming a single carrier model ($R_H = 1/n \times q$, where q is the electron charge). All selected samples showed negative Hall coefficient values indicating *n*-type semiconducting behavior. The carrier density of the Fe-free sample remains nearly constant (~ 80 x 10^{19} cm^{-3}) with rising temperature, as anticipated for a heavily doped semiconductor. At temperatures above 600 K, thermal activation of carriers from the valence band (VB) to the conduction band (CB) leads to marginal increase in the overall carrier density. Intriguingly, the incorporation of Fe into the HH matrix to develop FH nanoinclusions results in a reduction of the overall effective carrier concentration (*n*) for all samples, which is consistent with the observed drop in the electrical conductivity. The observed drop in *n* values is quite a surprising result since one would anticipate larger carrier concentration upon doping a semiconductor with a metallic phase. However, the observation is in agreement with previous studies where diminished overall carrier densities were found upon embedding nanoscale inclusions with full-Heusler (FH) structure into a half-Heusler (HH) matrix using excess elemental Ni.[28, 29] Such a change in the carrier density was rationalized using the concept of energy filtering of low-energy carriers at HH/FH interfaces, owing to the electronic energy band alignment offset between the neighboring phases. However, it was also found that the decrease in the carrier density due to energy filtering at the HH/FH interfaces strongly depends on the doping level of materials.[68] Only a marginal drop in the carrier density was found for heavily doped HH/FH composites containing a small fraction of low-energy carriers, such as the HH compositions under consideration in the present study. Therefore, the large drop in the carrier density upon increasing the Fe content (up to ~63% for the sample with x = 0.05) (**Figure 4c**) suggests that there must be an additional mechanism for electron "trapping" at play in these samples. For example, the large population density of magnetic (Ti,Fe)-rich FH nanoinclusions in $Ti_{0.25}Zr_{0.25}Hf_{0.5}(NiFe_{0.05})Sn_{0.975}Sb_{0.025}$ may act as trapping centers for itinerant charge carriers through a combination of the energy filtering effect at the matrix/inclusion interfaces,[36,37,42,67,68] and charge

localization by the magnetic nanoinclusions (**Figure 1c**). The localization of charge carriers around such magnetic (Ti,Fe)-rich FH nanoinclusions presumably leads to the formation of overlapping bound magnetic polarons (BMPs), resulting in the observed long-range ferromagnetic ordering up to T_c = 650 K and the large drop in the effective carrier density. Importantly, the charge carrier density for the sample with x = 0.05 remains nearly constant with the rising temperature up to ~ 650 K, above which a gradual increase in the carrier density is observed. This suggests that the loss of the FM ordering at temperatures above 650 K triggers the release of a fraction of initially trapped carriers into the electronic conduction. Further increase of the Fe content to 0.1 and 0.15 resulted in an increase in the carrier density compared to that of the sample with x = 0.05 (**Figure 4c**), suggesting partial doping of these samples due to the observed agglomeration of a large fraction of (Ti,Fe)-rich nanoinclusions into micrometer scale particles with bulk metallic conductivity.

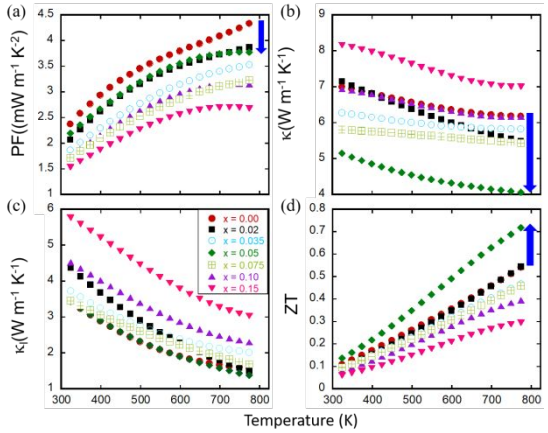

Figure 5: Thermoelectric properties of $Ti_{0.25}Zr_{0.25}Hf_{0.5}(Ni,Fe_x)Sn_{0.975}Sb_{0.025}$ composites: (a) power factor; (b) total thermal conductivity; (c) lattice thermal conductivity; and (d) thermoelectric figure of merit.

Remarkably, the drastic reduction in the carrier density of the sample with x = 0.05 resulted in a large increase in both the thermopower (**Figure 4b**) and the carrier mobility (**Figure 4d**). All samples showed negative thermopower values in the whole measured temperature range, further confirming the *n*-type semiconducting behavior of the synthesized composites. At 300 K, a ~42% increase in the thermopower (from -68 μV/K to -96 μV/K) was observed for the sample with x = 0.05 when compared to that of the Fe-free sample, with a ~22% enhancement at 775 K. The observed large increase in the thermopower offsets the reduction in the electrical conductivity. In addition, the 27 % increase in the carrier mobility (**Figure 4d**) partially compensates for the 63% reduction in the carrier concentration, leading to only a marginal decrease (13 % at 800 K) in the power factor (PF) (**Figure 5a**) for the composition with x = 0.05. Further increasing the Fe concentration above x = 0.05 leads to a decreasing power factor, mainly due to the degradation of the Seebeck coefficient.

The total thermal conductivity of the Fe-containing samples initially decreases with the increasing Fe content reaching minimum values for the sample with x = 0.05. At 300 K, the thermal conductivity of the Fe-free HH matrix is ~7 $Wm^{-1}K^{-1}$ and drops to ~ 5 $Wm^{-1}K^{-1}$ upon incorporation of 5 at% Fe. Additional Fe resulted in the total thermal conductivities larger than that of the Fe-free HH matrix. While the reduction in the total thermal conductivity of samples with x = 0.02, 0.035 and 0.05 is consistent with the observed trend in the electrical conductivity data, the measured larger total thermal conductivities for the samples with greater Fe contents are quite surprising. To fully understand the effect of nanostructuring on the total thermal conductivity of the synthesized samples, the electronic thermal conductivity (**Figure S6b**), calculated based on the Wiedemann–Franz law: $\kappa_e = L\sigma T$, where *L is* Lorenz number (2.45 x10^{-8} $W\Omega K^{-2}$ for degenerated semiconductors), σ is the electrical conductivity and T the absolute temperature, was subtracted from the total thermal conductivity. The resulting lattice contribution to the total thermal conductivity shown in **Figure 5c** reveals that Fe incorporation into $Ti_{0.25}Zr_{0.25}Hf_{0.5}NiSn_{0.975}Sb_{0.025}$ leads to composites with larger lattice thermal conductivity, except for the sample with x = 0.05, which maintains similar lattice thermal conductivity to that of the Fe-free HH matrix. The observed increase in the lattice thermal conductivity with increasing Fe content is consistent with the formation of interconnected (Ti,Fe)-rich FH inclusions with large thermal conductivity within the resulting composites, as shown from the SEM images (**Figure S3**). In the samples with x = 0.05, the (Ti,Fe)-rich FH nanoinclusions are widely dispersed, diminishing their contributions to the lattice thermal conductivity of the HH matrix. Therefore, the observed large reduction (33% at 800 K) in the total thermal conductivity for the sample with x = 0.05 compared to the Fe-free sample arises from the combination of low electronic thermal conductivity due to the substantial drop in the electrical conductivity and low lattice thermal conductivity owing to the dispersion of (Ti,Fe)-rich FH nanoinclusions within the HH matrix. Overall, the marginal decrease (13% at 800K) in the PF and the large reduction (33%) in the total thermal conductivity for the sample with x = 0.05 resulted in a significant (29%) improvement in the thermoelectric performance. A thermoelectric figure of merit, zT, as high as 0.75, was obtained at 775 K for the sample with x = 0.05, which corresponds to a marked enhancement compared to results previously reported for similar compositions at the same doping level.[47] The sharp slope of the zT plot points to even higher values at higher temperatures.

Conclusion

In summary, we demonstrate that starting from a half-Heusler thermoelectric material with fully optimized doping level, $Ti_{0.25}Zr_{0.25}Hf_{0.5}NiSn_{0.975}Sb_{0.025}$, further enhancement of the figure of merit can be achieved through incorporation of widely dispersed coherent atomic scale magnetic nanoinclusions within the matrix. The incorporation of magnetic nanoinclusions within the HH matrix is achieved through preferential reactivity of the added elemental Fe atoms with Ti to form (Ti,Fe)-rich ($TiNi_{4/3}Fe_{2/3}Sn$) nanoinclusions with FH structure coherently embedded within the (Zr,Hf)-rich HH matrix. We found that such atomic scale magnetic FH inclusions regulate the electronic behavior of the existing ensembles of electrons by trapping a significant fraction of itinerant charge carriers via (1) energy filtering at the matrix/inclusion interfaces and, more importantly, through (2) magnetic coupling interactions between localized moments of embedded FH inclusions and the spins of the free carriers, resulting in a large reduction in the effective carrier density. The atomic scale engineering of electronic transport within the HH matrix using magnetic nanoinclusions has the following three major consequences. First, the localization of itinerant carriers by the magnetic nanoinclusions results in the formation of overlapping bound magnetic polarons (BMPs), inducing a high T_c ~ 650 K diluted ferromagnetic semiconductor. Secondly, the large reduction in the effective carrier density gives rise to a significant enhancement of both the carrier mobility and thermopower, which minimizes detriment to the overall power factor. Finally, the decreased electrical conductivity arising from the diminished effective carrier concentration causes a significant drop in the total thermal conductivity, owing to the reduction of the electronic contribution to the thermal conductivity. The discovery of this novel approach to enhance the thermoelectric figure of merit using coherent magnetic nanoinclusions is expected to pave the way towards even larger figures of merit in leading thermoelectric materials.

AUTHOR INFORMATION

Corresponding Author

* Correspondence to: ppoudeup@umich.edu

Author Contributions

R.L. synthesized the samples, carried out structural characterization, performed the SEM characterization, performed high temperature electronic and thermal conductivity measurements, performed data analysis, and co-wrote the manuscript. J.L. performed magnetic measurements, performed data analysis, and co-edited the manuscript. Y.L. synthesized the samples, carried out structural characterization and co-edited the manuscript. T.P.B., A.A.P., S. W. and C.U. performed high temperature Hall effect, electrical conductivity and Seebeck coefficient measurements and co-edited the manuscript. P.F.P.P. conceived the experiment, performed data analysis and co-wrote the manuscript.

Notes

The authors declare no competing financial interest.

ACKNOWLEDGMENT

This work was supported by the Department of Energy, Office of Basic Energy Sciences under Award # DE-SC-0008574 and DE-SC-0018941. PFPP also gratefully acknowledges financial support from the National Science Foundation under Awards DMR-1237550 and DMR-1561008. Magnetic data were recorded on SQUID magnetometers at the University of Michigan purchased using MRI grants from the NSF (DMR- 1428226 and CHE-104008). This work made use of the TEM from the Michigan Materials Characterization Center, $(MC)^2$, purchased with funds from the National Science Foundation Awards (DMR-0723032).

REFERENCES

[1] Rowe D.M. Thermoelectrics handbook: macro to nano; CRC press, 2005.
[2] Dresselhaus M.S.; Chen G.; Tang M.Y.; Yang R.; Lee H.; Wang D.; Ren Z.; Fleurial J.P.; Gogna P. Advanced Materials **2007**, 19, 1043.
[3] Minnich A.; Dresselhaus M.; Ren Z.; Chen G. Energy & Environmental Science **2009**, 2, 466.
[4] Thompson D. **2012**.
[5] Poudel B.; Hao Q.; Ma Y.; Lan Y.; Minnich A.; Yu B.; Yan X.; Wang D.; Muto A.; Vashaee D. Science **2008**, 320, 634.
[6] Kim W.; Zide J.; Gossard A.; Klenov D.; Stemmer S.; Shakouri A.; Majumdar A. Physical Review Letters **2006**, 96, 045901.
[7] Wang X.; Lee H.; Lan Y.; Zhu G.; Joshi G.; Wang D.; Yang J.; Muto A.; Tang M.; Klatsky J. Applied Physics Letters **2008**, 93, 193121.
[8] Joshi G.; Lee H.; Lan Y.; Wang X.; Zhu G.; Wang D.; Gould R.W.; Cuff D.C.; Tang M.Y.; Dresselhaus M.S. Nano Letters **2008**, 8, 4670.
[9] Xie W.; Tang X.; Yan Y.; Zhang Q.; Tritt T.M. Journal of Applied Physics **2009**, 105, 113713.
[10] Li H.; Tang X.; Zhang Q.; Uher C. Applied Physics Letters **2008**, 93, 252109.
[11] Snyder G.J.; Toberer E.S. In *Materials For Sustainable Energy: A Collection of Peer-Reviewed Research and Review Articles from Nature Publishing Group*; World Scientific: 2011, p 101.
[12] Snyder G.J.; Christensen M.; Nishibori E.; Caillat T.; Iversen B.B. Nature Materials **2004**, 3, 458.
[13] Nolas G.; Morelli D.; Tritt T.M. Annual Review of Materials Science **1999**, 29, 89.
[14] Cahill D.G.; Watson S.K.; Pohl R.O. Physical Review B **1992**, 46, 6131.
[15] Kurosaki K.; Kosuga A.; Muta H.; Uno M.; Yamanaka S. Applied Physics Letters **2005**, 87, 061919.
[16] Bux S.K.; Zevalkink A.; Janka O.; Uhl D.; Kauzlarich S.; Snyder J.G.; Fleurial J.-P. Journal of Materials Chemistry A **2014**, 2, 215.
[17] Morelli D.; Jovovic V.; Heremans J. Physical Review Letters **2008**, 101, 035901.
[18] Shi X.; Yang J.; Salvador J.R.; Chi M.; Cho J.Y.; Wang H.;

Bai S.; Yang J.; Zhang W.; Chen L. Journal of the American Chemical Society **2011**, 133, 7837.
[19] Schmitt D.C.; Haldolaarachchige N.; Xiong Y.; Young D.P.; Jin R.; Chan J.Y. Journal of the American Chemical Society **2012**, 134, 5965.
[20] Wu D.; Zhao L.-D.; Tong X.; Li W.; Wu L.; Tan Q.; Pei Y.; Huang L.; Li J.-F.; Zhu Y. Energy & Environmental Science **2015**, 8, 2056.
[21] Sharp J.W.; Sales B.C.; Mandrus D.G.; Chakoumakos B.C. Applied Physics Letters **1999**, 74, 3794.
[22] Polman A.; Atwater H.A. Nature Materials **2012**, 11, 174.
[23] Green M.A. Progress in Photovoltaics: Research and Applications **2001**, 9, 123.
[24] Biswas K.; He J.; Zhang Q.; Wang G.; Uher C.; Dravid V.P.; Kanatzidis M.G. Nature Chemistry **2011**, 3, 160.
[25] Li J.-F.; Liu W.-S.; Zhao L.-D.; Zhou M. NPG Asia Materials **2010**, 2, 152.
[26] Pei Y.; Wang H.; Snyder G.J. Advanced Materials **2012**, 24, 6125.
[27] Pei Y.; Shi X.; LaLonde A.; Wang H.; Chen L.; Snyder G.J. Nature **2011**, 473, 66.
[28] Liu W.; Tan X.; Yin K.; Liu H.; Tang X.; Shi J.; Zhang Q.; Uher C. Physical Review Letters **2012**, 108, 166601.
[29] Tan G.; Zhao L.-D.; Shi F.; Doak J.W.; Lo S.-H.; Sun H.; Wolverton C.; Dravid V.P.; Uher C.; Kanatzidis M.G. Journal of the American Chemical Society **2014**, 136, 7006.
[30] Hicks L.; Dresselhaus M.S. Physical Review B **1993**, 47, 16631.
[31] Yu B.; Zebarjadi M.; Wang H.; Lukas K.; Wang H.; Wang D.; Opeil C.; Dresselhaus M.; Chen G.; Ren Z. Nano Letters **2012**, 12, 2077.
[32] Zebarjadi M.; Joshi G.; Zhu G.; Yu B.; Minnich A.; Lan Y.; Wang X.; Dresselhaus M.; Ren Z.; Chen G. Nano Letters **2011**, 11, 2225.
[33] Pei Y.-L.; Wu H.; Wu D.; Zheng F.; He J. Journal of the American Chemical Society **2014**, 136, 13902.
[34] Vashaee D.; Shakouri A. Physical Review Letters **2004**, 92, 106103.
[35] Heremans J.P.; Thrush C.M.; Morelli D.T. Physical Review B **2004**, 70, 115334.
[36] Makongo J.P.; Misra D.K.; Zhou X.; Pant A.; Shabetai M.R.; Su X.; Uher C.; Stokes K.L.; Poudeu P.F. Journal of the American Chemical Society **2011**, 133, 18843.
[37] Liu Y.; Sahoo P.; Makongo J.P.; Zhou X.; Kim S.-J.; Chi H.; Uher C.; Pan X.; Poudeu P.F. Journal of the American Chemical Society **2013**, 135, 7486.
[38] Tsujii N.; Mori T. Applied Physics Express **2013**, 6, 043001.
[39] Tsujii N.; Mori T.; Isoda Y. Journal of Electronic Materials **2014**, 43, 2371.
[40] Zhao W.; Liu Z.; Wei P.; Zhang Q.; Zhu W.; Su X.; Tang X.; Yang J.; Liu Y.; Shi J. Nature Nanotechnology **2017**, 12, 55.
[41] Zhao W.; Liu Z.; Sun Z.; Zhang Q.; Wei P.; Mu X.; Zhou H.; Li C.; Ma S.; He D. Nature **2017**, 549, 247.
[42] Sahoo P.; Liu Y.; Makongo J.P.; Su X.-L.; Kim S.J.; Takas N.; Chi H.; Uher C.; Pan X.; Poudeu P.F. Nanoscale **2013**, 5, 9419.
[43] Kimura Y.; Tanoguchi T.; Sakai Y.; Chai Y.-W.; Mishima Y. MRS Online Proceedings Library Archive **2011**, 1295.
[44] Chai Y.W.; Yoshioka K.; Kimura Y. Scripta Materialia **2014**, 83, 13.
[45] Kimura Y.; Chai Y.-W. JOM **2015**, 67, 233.
[46] Kenjo T.; Kimura Y.; Mishima Y. MRS Online Proceedings Library Archive **2009**, 1218.
[47] Culp S.; Poon S.; Sorloaica N.; Tritt T. In *Thermoelectrics, 2005. ICT 2005. 24th International Conference on*; IEEE: 2005, p 384.
[48] Joshi G.; Dahal T.; Chen S.; Wang H.; Shiomi J.; Chen G.; Ren Z. Nano Energy **2013**, 2, 82.
[49] Page A.; Van der Ven A.; Poudeu P.; Uher C. Journal of Materials Chemistry A **2016**, 4, 13949.
[50] Berche A.; Tédenac J.; Jund P. Scripta Materialia **2017**, 139, 122.
[51] Gałązka K.; Populoh S.; Sagarna L.; Karvonen L.; Xie W.; Beni A.; Schmutz P.; Hulliger J.; Weidenkaff A. Physica Status Solidi (a) **2014**, 211, 1259.
[52] Geng H.; Zhang H. Journal of Applied Physics **2014**, 116, 033708.
[53] Goodenough J.B. Journal of Physics and Chemistry of Solids **1958**, 6, 287.
[54] Djieutedjeu H.; Poudeu P.F.; Takas N.J.; Makongo J.P.; Rotaru A.; Ranmohotti K.G.; Anglin C.J.; Spinu L.; Wiley J.B. Angewandte Chemie International Edition **2010**, 49, 9977.
[55] Ranmohotti K.G.; Djieutedjeu H.; Lopez J.; Page A.; Haldolaarachchige N.; Chi H.; Sahoo P.; Uher C.; Young D.; Poudeu P.F. Journal of the American Chemical Society **2015**, 137, 691.
[56] Yamamoto S.; Fukui T.; Maisinger K.; Schollwöck U. Journal of Physics: Condensed Matter **1998**, 10, 11033.
[57] Terashita H.; Neumeier J. Physical Review B **2005**, 71, 134402.
[58] Pillai S.S.; Rangarajan G.; Raju N.; Epstein A.; Santhosh P. Journal of Physics: Condensed Matter **2007**, 19, 496221.
[59] Torrance J.; Shafer M.; McGuire T. Physical Review Letters **1972**, 29, 1168.
[60] Lascaray J.; Desfours J.; Averous M. Solid State Communications **1976**, 19, 677.
[61] Sawicki M.; Dietl T.; Kossut J.; Igalson J.; Wojtowicz T.; Plesiewicz W. Physical Review Letters **1986**, 56, 508.
[62] Berciu M.; Bhatt R. Physical Review Letters **2001**, 87, 107203.
[63] Kaminski A.; Sarma S.D. Physical Review Letters **2002**, 88, 247202.
[64] Sarma S.D.; Hwang E.; Kaminski A. Physical Review B **2003**, 67, 155201.
[65] Coey J.; Venkatesan M.; Fitzgerald C. Nature Materials **2005**, 4, 173.
[66] Moroz N.A.; Lopez J.S.; Djieutedjeu H.; Ranmohotti K.G.; Olvera A.; Ren P.; Page A.; Takas N.J.; Uher C.; Poudeu P.F. Chemistry of Materials **2016**, 28, 8570.
[67] Makongo J.P.; Misra D.K.; Salvador J.R.; Takas N.J.; Wang G.; Shabetai M.R.; Pant A.; Paudel P.; Uher C.; Stokes K.L. Journal of Solid State Chemistry **2011**, 184, 2948.
[68] Liu Y.; Makongo J.P.; Page A.; Sahoo P.; Uher C.; Stokes K.; Poudeu P.F. Journal of Solid State Chemistry **2016**, 234, 72.

Table of Contents artwork

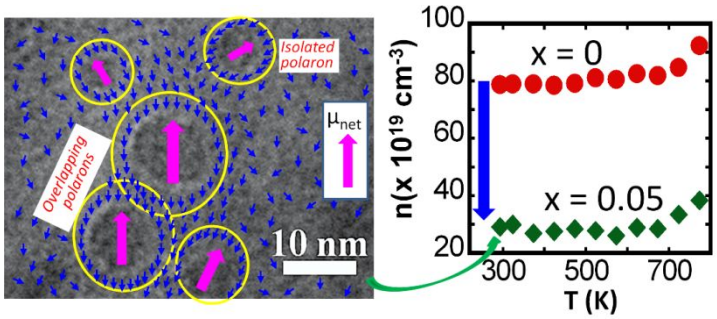

Coherent incorporation of magnetic nanoinclusions into a heavily doped semiconductor induces charge localization and formation of overlapping bound magnetic polarons leading to drastic reduction of the effective carrier density, high *Tc* ferromagnetism and improved thermoelectric performance.

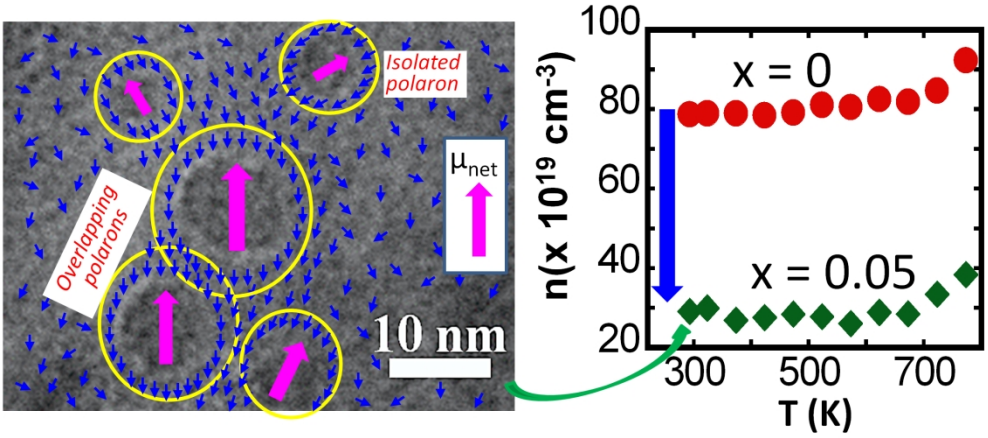

212x92mm (300 x 300 DPI)